

ARTICLE OPEN

Dual-species, multi-qubit logic primitives for Ca^+/Sr^+ trapped-ion crystalsC. D. Bruzewicz^{1*}, R. McConnell¹, J. Stuart², J. M. Sage^{1,2} and J. Chiaverini^{1*}

We demonstrate key multi-qubit quantum-logic primitives in a dual-species trapped-ion system based on $^{40}\text{Ca}^+$ and $^{88}\text{Sr}^+$ ions, using two optical qubits with quantum-logic-control frequencies in the red to near-infrared range. With all ionization, cooling, and control wavelengths in a wavelength band similar for the two species and centered in the visible, and with a favorable mass ratio for sympathetic cooling, this pair is a promising candidate for scalable quantum information processing. Same-species and dual-species two-qubit gates, based on the Mølmer-Sørensen interaction and performed in a cryogenic surface-electrode trap, are characterized via the fidelity of generated entangled states; we achieve fidelities of 98.8(2)% and 97.5(2)% in Ca^+-Ca^+ and Sr^+-Sr^+ gates, respectively. For a similar Ca^+-Sr^+ gate, we achieve a fidelity of 94.3(3)%, and carrying out a Sr^+-Sr^+ gate performed with a Ca^+ sympathetic cooling ion in a $\text{Sr}^+-\text{Ca}^+-\text{Sr}^+$ crystal configuration, we achieve a fidelity of 95.7(3)%. These primitives form a set of trapped-ion capabilities for logic with sympathetic cooling and ancilla readout or state transfer for general quantum computing and communication applications.

npj Quantum Information (2019)5:102; <https://doi.org/10.1038/s41534-019-0218-z>

INTRODUCTION

Quantum computing requires ancilla qubits as crucial components of quantum algorithmic primitives, such as quantum phase estimation,¹ gate teleportation,² and syndrome extraction during quantum error correction.³ In addition, particular physical implementations of quantum information processing (QIP) may utilize additional physical qubits to aid in the preparation, transport, and readout of quantum information. Particularly for trapped-ion qubits, one of the most promising quantum-computing modalities,^{4–7} quantum-logic operations on chains containing both computational and ancilla ions are a critical component of practical QIP systems.

In such systems, computational ions, which house the qubits primarily used for quantum-logic operations, will likely be paired with ancilla ions of a different species such that control fields applied to the ancilla ions will not affect or decohere the quantum states of the computational ions.^{8,9} An alternate single-species strategy based on shelving a subset of the ion register in nearby levels outside of the qubit state subspace during certain quantum operations has been successfully demonstrated.¹⁰ Although the shelving technique added a tolerable number of additional operations in that work, it would likely require significant additional overhead when manipulating large qubit registers. In a system equipped with multiple atomic species, however, ancillas could be used for sympathetic cooling,^{9,11} for remote-entanglement generation using photons at fiber-friendly wavelengths,¹² or for ancilla-qubit readout without decoherence of unmeasured qubits due to scattered fluorescence photons¹³—all without the need for shelving operation overhead. Although different isotopes of the same element can provide some isolation, the isotope shifts of the relevant transitions are not typically large enough to reach levels required for high-fidelity quantum operations, much less fault tolerance. Desired properties of ion species pairs used for QIP include a high-coherence controllable qubit in the computational ion, similar masses of the

computational and ancilla ions to allow efficient energy transfer for sympathetic cooling,^{8,14} and favorable control frequencies in both species. Control should be favorable not only in regards to the absolute frequency but also to overlap of the frequency ranges required for the two species. Especially in light of the potential use of integrated technologies for control-light distribution in trapped-ion quantum processors,^{15–18} ion pairs with similar control wavelengths in the visible to near-infrared portion of the spectrum may be preferable to minimize coupling and propagation losses in the optical components,¹⁹ while also keeping the number of different material systems needed to work across the required wavelength range to a minimum.

Here we demonstrate a set of quantum-logic primitives, using the $^{40}\text{Ca}^+/\text{Sr}^+$ two-species system, which form the basis for a possible QIP architecture. Each of these ions houses a long-lived, optical-frequency qubit that has proven to be a workhorse for demanding QIP experiments and demonstrations.^{20,21} Their mass ratio near 2 allows for efficient momentum transfer for sympathetic cooling. Furthermore, the wavelengths required for production, cooling, logic, and readout in each species fall in the optical and near-infrared range, and their respective ranges have a high degree of overlap, minimizing required additional considerations for optical materials, etc., in the case of dual-species operation. Moreover, using these two optical qubits, the frequencies of control fields required for quantum logic, where the highest intensities and phase stability are required, are at very favorable wavelengths (729 nm and 674 nm for Ca^+ and Sr^+ , respectively) for laser and optical component technology. As an additional benefit, light emitted by broad transitions in these species, as would be used for remote-entanglement generation, is in the blue and infrared parts of the spectrum. Collection, distribution, and controlled interference of this light is considerably simpler than when manipulating light from similar transitions in the ultraviolet. Moreover, the light from these broad transitions in Ca^+ and Sr^+ is also sufficiently separated in frequency to not

¹Lincoln Laboratory, Massachusetts Institute of Technology, Lexington, Massachusetts 02421, USA. ²Massachusetts Institute of Technology, Cambridge, Massachusetts 02139, USA. *email: colin.bruzewicz@ll.mit.edu; john.chiaverini@ll.mit.edu

appreciably affect the coherence of nearby ions of the other species.²² Our demonstration of a suite of two-qubit quantum-logic primitives using two optical-frequency qubits helps establish this ion-species pair as a useful system for scalable-QIP explorations.

Prior work in dual-species trapped-ion quantum logic includes demonstrations of so-called quantum-logic spectroscopy²³ to enable the operation of optical clocks using ions with inaccessible or inconvenient transitions; these typically focus on the Al^+ clock ion with another species similar in mass used to manipulate and read out its state.²⁴ Entangling quantum gates have also been performed with the ion systems Be^+/Mg^+ ,¹³ Be^+/Ca^+ ,²⁵ $^{40}\text{Ca}^+/\text{Ca}^+$,²⁶ and Ba^+/Yb^+ .²⁷ Although these pairs will likely find particular application, they all have drawbacks, such as technologically challenging wavelengths, insufficient separation in internal-state energy splittings, or large masses, and so it is beneficial to explore alternative dual-species systems that may have complementary strengths.

The Ca^+/Sr^+ system has been considered recently for applications in QIP, although few quantum-logic operations in the combined system have been reported. For instance, these species form the basis of several analyses of large-scale quantum computing platforms, both as sympathetic cooling ancillas⁶ and for photon-emitting intermediaries in optically linked architectures;²⁸ a method has also been suggested to perform an interspecies gate in the Ca^+/Sr^+ system using a single laser wavelength.²⁶ Although considerable work demonstrating same-species, two-qubit operations in Ca^+ ^{20,29–32} and, to a lesser extent, Sr^+ ^{21,33} exists, their use together has not been investigated widely. Due to its potential utility, it is important to explore the implications of quantum operations based on this species pair.

Architectural components

One potential architecture for QIP with trapped ions consists of a two-dimensional array of trapping zones, interconnected via transport regions, in which two species of ions are held^{9,34} (see Fig. 1a). Each trapping zone holds a few-ion, one-dimensional ion crystal, in which multi-qubit operations can be performed. Ions are moved between trapping zones via the transport regions to bring ions from different array sites into the same crystal, such that a high degree of connectivity of multi-qubit operations can be

maintained across the array, limited only by the complexity of the transport region network. Housing one to four ions in each site simplifies the vibrational-mode spectrum when compared with keeping all ions in one crystal, while potentially permitting simultaneous individual addressing of many ions throughout an array. Ion crystals composed of ions from separate array sites, transported and then joined together, may acquire vibrational-mode excitation that can limit gate fidelity. Hence, any array site where multi-qubit gate operations will be performed contains one or two ancilla ions used primarily for sympathetic cooling prior to gate operations, allowing preparation of select vibrational modes of the crystal without affecting the internal state of the computational ions.

Such an architecture could be flexible in terms of application. The segmented trap structure can be tailored in terms of connectivity from nearest-neighbor, e.g., for surface-code quantum-error correction or quantum emulation of solid-state Hamiltonians, to fully connected, e.g., for quantum chemistry simulations requiring Jordan–Wigner transformations between qubit and orbital bases. The connectivity can also be reconfigured dynamically to suit the particular entanglement-generation requirements of a quantum algorithm as it proceeds. In all these cases, however, the composition of each array site can be essentially identical, able to maintain one to two of each of the computational ions and ancilla ions in a linear crystal. We focus here on demonstrations of key two-qubit primitives that enable operations within these individual sites, e.g., architectural components useful for multiple applications, using the Ca^+/Sr^+ system.

Basic two-qubit logic between ions of the same species forms the foundation of any QIP application that requires entanglement generation or qubit interaction, and we therefore begin with Ca^+-Ca^+ and Sr^+-Sr^+ two-qubit gates, which set the baseline capability of this system. These gates lead naturally to an architectural primitive in which a gate is performed between two ions of a single species in the presence of a sympathetic coolant ancilla of a second species. This operation would be the primary multi-qubit gate in a case in which all array sites contain a single computational ion, while a subset of the sites also contain a co-located coolant ancilla. To perform logic operations between pairs of computational ions, a lone computational ion is transported from its home site to the home site of a

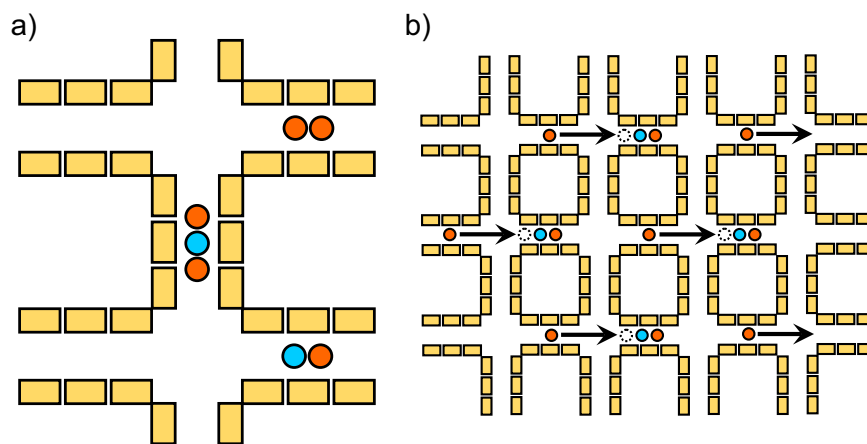


Fig. 1 Trap array architecture with ion-transport-based connectivity. **a** Subsection of array showing segmented electrodes that create both static potential wells at multiple array sites and dynamically variable potentials for ion transport. Different zones depict various crystal configurations of computational ions (red) and ancilla ions (blue). **b** A larger section of such an array configured for quantum computation with surface-code error correction encoding; in this case, two-qubit gates are performed between nearest-neighbor computational ions after transporting lone computational ions to the zones (alternating in a checkerboard pattern) where a computational ion is housed with an ancilla. One step in the error-correction cycle is depicted. The ancilla is used to prepare the shared motional state before gate operations and the ancilla could also be used for periodic syndrome readout without detrimental effect on unmeasured computational ions due to photon scattering

computational ion which houses an ancilla. All three ions are then joined in a single crystal. The ancilla is used to remove any unwanted motional excitation accrued during ion movement and crystal merging (the opposite operation, crystal separation, will in general occur before the next gate involving one of the current computational ions, and sympathetic cooling via an ancilla subsequent to transport and merging will also remove the kinetic energy acquired during this process). The gate is then performed between the computational ions. As a particular example, the surface code³⁵ can be implemented in such an architectural scheme in which half the sites, in a checkerboard pattern, of a square array contain sympathetic-cooling ancillas (see Fig. 1b). Here we demonstrate each of the above-mentioned same-species, multi-ion, quantum-logic architectural components.

Dual-species operations provide additional key capabilities for trapped-ion-based quantum information processors and therefore form other primitives of interest. For instance, in a larger-scale system employing quantum error correction, subsets of the qubits must be measured during the computation. Moreover, measurement-based quantum computing also requires projecting a subset of qubits while maintaining coherence of the unmeasured remainder. In both cases, inter-species transfer of state population to ancillas just prior to measurement can avoid decoherence in computational ions due to resonant light scattered from measured ions in close proximity.²² Another important example is repeat-until-success remote-entanglement generation for linking modules of a composite quantum information processor;²⁷ in this case, ions desired for long-distance communication, either due to particular wavelengths or beneficial level structures, may be different from the computational species. Transfer of the quantum state from a computational ion to one qubit of a Bell-entangled ancilla pair can allow for independent choices of ion species in these roles. For instance, a different communication-ion species may be desirable to enhance overall processor speed without affecting the coherence of neighboring computational ions during repeated entanglement-generation attempts. In contrast to the shelving of same-species computational-ion qubits to protect them from incident resonant photons, using a second species permits execution of logic operations and entanglement generation in parallel.

Transfer to ancillas to avoid decoherence during measurement does not necessarily need to preserve qubit phase information, and hence techniques based on quantum-logic spectroscopy^{23,36} can be utilized to accomplish this readout scheme. A full phase-preserving state swap, e.g., a series of three CNOT gates based on a dual-species entangling gate, can also fulfill this task;¹³ for state transfer into part of a remote entangled pair as a prerequisite for additional computation, only full quantum-state transfer will suffice. We have previously performed quantum-logic-assisted readout of a Ca^+ ion using a Sr^+ ion,²² a technique that may be useful for resonant-light-scatter-free syndrome extraction in a close-packed array. This operation required a pair of π -pulses on the sideband transitions corresponding to a shared vibrational mode after it was cooled to the ground state. Here we demonstrate a more general dual-species Mølmer-Sørensen (MS) entangling gate between Ca^+ and Sr^+ , a method that has an advantage beyond phase preservation in that ground-state cooling is generally not required for MS gates.²⁹ It could therefore be used for both syndrome extraction and remote-entanglement-generation applications.

RESULTS

Experimental procedures

We confine and manipulate $^{40}\text{Ca}^+$ and $^{88}\text{Sr}^+$ ions in a linear surface-electrode trap consisting of a $2\ \mu\text{m}$ -thick, patterned aluminum layer on a sapphire substrate, similar to traps used in

previous work.^{37,38} Single-ion axial trap frequencies in the 0.5–2 MHz range are produced via application of potentials to segmented electrodes defined along the axial direction; radial trapping at frequencies near 5 MHz is produced through application of a radiofrequency (RF) potential near 50 MHz to a subset of the electrodes. Ions are held $50\ \mu\text{m}$ from the trap-chip surface in a cryogenic vacuum chamber achieving ultra-high vacuum pressure in which the trap is maintained at a temperature below 6 K. The ions are loaded into the trap via photoionization from neutral atomic beams produced via acceleration from co-located Ca and Sr two-dimensional magneto-optical traps to the remotely located trap chip.^{22,39}

Environmental magnetic-field fluctuations are suppressed using a pair of superconducting niobium rings⁴⁰ located above and below the trap chip. The rings are centered radially on the ion location, with one 10 mm-square ring attached just beneath the trap's sapphire substrate and one 65 mm-diameter octagonal ring attached to the radiation shield $\sim 5\ \text{mm}$ from the trap surface; this design is shown schematically in Fig. 2a. Induced supercurrents in the rings compensate variation in the local magnetic field⁴¹ in the direction of an applied, axial quantizing field of $\sim 5 \times 10^{-4}\ \text{T}$. In practice, the quantizing magnetic field is produced using the supercurrent induced in the rings. To reduce field noise, the current in coils used to inject this supercurrent is removed once the rings are in the superconducting state. We have measured suppression of slow magnetic-field fluctuations by a factor of 17–20 dB using this technique.

Qubits are defined using the electronic states in each ion, with an optical-frequency separation between the $|0\rangle \equiv |(n-1)^2D_{5/2}, m_J = -5/2\rangle$ and $|1\rangle \equiv |n^2S_{1/2}, m_J = -1/2\rangle$ states, where $n = \{4, 5\}$ for $\{\text{Ca}^+, \text{Sr}^+\}$. Light for qubit manipulation and multi-qubit operations is derived from separate systems each consisting of an external-cavity-stabilized diode laser, frequency locked to an ultra-low-expansion glass cavity. Transmitted light, filtered by the cavity, is used to injection-lock one or more slave diode lasers²¹ and the output is amplified via one or more tapered optical amplifiers. Light is passed through several acousto-optic modulators (AOMs) to shift the frequency and modulate the amplitude and phase (and frequency for multi-qubit operations) before being delivered to the ions through windows in the vacuum chamber. Beam paths are shown in Fig. 2b.

Experimental trials each begin with Doppler cooling of the ions using light at 397 nm (422 nm) in conjunction with repumping light at 866 nm (1092 nm) for Ca^+ (Sr^+); the same construction will be used throughout this paragraph. Light at 854 nm (1033 nm) is also applied to quench any residual population in $|0\rangle$ through the $n^2P_{3/2}$ level. Ions are Doppler cooled for $\sim 1\ \text{ms}$, after which resolved sideband cooling is performed to bring the ions to the motional ground state for a subset of the axial vibrational modes of the ions in the crystal. For same-species, two-qubit gates with two ions in the crystal, sideband cooling pulses at 729 nm (674 nm) interspersed with quenching pulses at 854 nm (1033 nm) are used to bring the in-phase (IP) and out-of-phase (OOP) modes (see Fig. 2c) to average occupation below ~ 0.05 . Sideband cooling for dual-species, two-qubit gates and single-species, three-ion, two-qubit gates will be described below in the respective sections. Optical pumping after sideband cooling serves as state preparation, bringing the ions to $|1\rangle$ using a combination of 729 nm and 854 nm (674 nm and 1033 nm) light. After state preparation, bichromatically modulated light is used to perform two-qubit entangling operations via the MS technique.⁴²

State detection is performed by applying the wavelengths used for Doppler cooling, but without the quench light, such that an ion in $|1\rangle$ will fluoresce at 397 nm (422 nm), whereas an ion in $|0\rangle$ will not. Fluorescence is collected using a high-numerical-aperture objective outside the vacuum chamber and directed to an electron multiplying charge-coupled device or photo-multiplier tube (PMT) for imaging or state detection, respectively. For single-

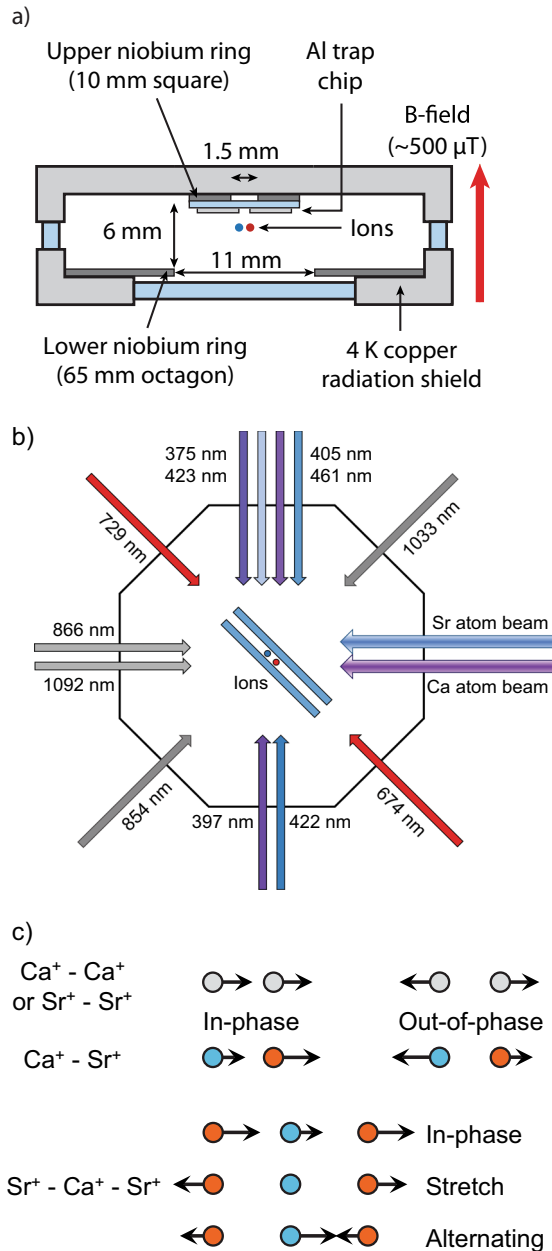


Fig. 2 Magnetic-field shielding, laser beam paths, and ion-crystal motional modes. **a** Self-shielding, superconducting ring geometry for suppressing magnetic-field noise. Fluctuations in the magnetic flux threading the rings induce persistent supercurrents that (partially) cancel the changes in magnetic flux. **b** Top view of the beam paths in the ion-trapping chamber. Arrows are offset in the figure for clarity, but the beams are largely overlapped in the experimental apparatus. **c** Ion-crystal configurations and axial normal vibrational modes pertaining to two- and three-ion chains employed in this work. Arrows (not drawn to scale) indicate the relative amplitudes and directions of the normalized motional eigenvectors for the different ion crystals

species gates, ions are detected simultaneously and the detection time, typically a few milliseconds, is set such that experimental photon-number histograms corresponding to 0, 1, or 2 ions in the scattering $|1\rangle$ state are sufficiently separated to allow discrimination between these cases with error probability below ~ 0.001 . It is noteworthy that of the four possible two-qubit state outcomes, two of them are indistinguishable when measured using the non-

imaging PMT; hence, only the sum of the probabilities for the states $|01\rangle$ and $|10\rangle$ are measured. This is not a limitation for determination of the fidelities of the created Bell states, as only the populations of the $|00\rangle$ and $|11\rangle$ states, and the parity of the two-qubit state measured in an auxiliary experiment performed on the Bell state, are needed.⁴³ In the mixed-species gate, fluorescence is detected from each ion sequentially, but the fidelity is calculated in the same way as in the single-species gates.

Mølmer-Sørensen logic gates and considerations pertaining to ion crystal configuration and motional modes

The MS gates demonstrated here are enacted through optical dipole forces applied at frequencies near a particular shared motional mode of the trapped-ion crystal. When bringing about these forces via a bichromatic light field with frequency components detuned by δ above and below the blue and red motional sidebands (mode frequency ω_β), the interaction Hamiltonian for two ions is⁴⁴

$$H_I(t) = \hbar\Omega \left(e^{-i(\omega_\beta + \delta)t} + e^{i(\omega_\beta + \delta)t} \right) e^{i\eta(ae^{-i\omega_\beta t} + a^\dagger e^{i\omega_\beta t})} \left(\sigma_+^{(1)} + \sigma_+^{(2)} \right) + \text{h.c.} \quad (1)$$

Here a is the annihilation operator of the vibrational mode of interest, Ω is the $|1\rangle \rightarrow |0\rangle$ transition Rabi frequency, $\sigma_+^{(j)}$ is the raising operator for the electronic spin qubit of ion j defined via the Pauli spin operators as $\sigma_+ = (\sigma_x + i\sigma_y)/2$, and $\eta = k z_{\text{RMS}}$ is the Lamb-Dicke parameter, which expresses the ratio between the vibrational ground-state wavefunction size $z_{\text{RMS}} = \sqrt{\hbar/(2m\omega_\beta)}$ and the spatial gradient of the electromagnetic field, as expressed by the mode-direction projection of the wavevector k of the light used to drive the transition. We are here assuming a single-species MS gate for simplicity; below we generalize the Lamb-Dicke parameter to more complex configurations. Taking the rotating-wave approximation and in the Lamb-Dicke limit ($\eta\sqrt{\langle (a + a^\dagger)^2 \rangle} \ll 1$), this Hamiltonian becomes

$$H_I(t) = -\hbar\eta\Omega (ae^{-i\delta t} + a^\dagger e^{i\delta t}) \left(\sigma_y^{(1)} + \sigma_y^{(2)} \right). \quad (2)$$

This interaction couples the motional mode to the joint spin state of the two ions, and by driving off-resonance with detuning δ , the vibrational mode acquires a geometric phase that depends on the joint spin state as it traverses a curved path in the phase space of the mode. At drive times equal to multiples of $t_g = 2\pi/\delta$, the curved path becomes a closed loop and the ions' spin and motion are disentangled, while a subset of the two-ion spin states acquire a phase relative to the others; by setting the interaction strength such that $\eta\Omega = \delta/4$, a maximally (spin) entangled state can be created after a time t_g .

The mode structure affects the gate time through the Lamb-Dicke parameter, but this is rather straightforward in same-species gates. We now discuss considerations affecting the gate time for dual-species operations, where the Lamb-Dicke parameter is ion-dependent, and we consider errors due to excitation of spectator modes spectrally close to the gate-drive frequency, an effect that can be exacerbated in mixed-species systems. See Methods for the calculation of the mode structure in dual-species crystals.

In general, it is desirable to execute multi-qubit operations in the shortest possible time with the highest possible fidelity, and both of these design goals can be affected by the chosen motional mode used to execute the gate. For the optical qubits used here, the attainable sideband Rabi frequencies, which set the MS gate time, are determined by the electric quadrupole transition matrix elements between the chosen qubit states, the Lamb-Dicke parameters for the relevant motional mode, and the qubit laser intensities. These parameters can easily be made, to a very good approximation, equal for ions of the same species. In multi-species crystals, however, the values can vary significantly and each must be well characterized to achieve high-fidelity

operation. For example, the electric quadrupole transition matrix element for the chosen qubit states in Ca^+ is ~ 0.7 times that of Sr^+ .⁴⁵ As shown in Methods, the Lamb-Dicke parameters vary for different ion species in different motional modes using different crystal configurations. The sideband Rabi frequencies can be equalized, however, by adjusting the gate-laser intensities at the ion locations, subject to the constraints imposed by the available laser power and the achievable beam waists. We also point out that the inclusion of a second atomic species in three-ion crystals brings about additional considerations, as each ion crystal configuration yields different normal mode frequencies and motional amplitudes.

In addition to affecting the gate speed, motional mode choice can also determine the sensitivity of the ion chain to different types of electric-field noise. Homogeneous electric fields couple most strongly to IP motional modes. Hence, some level of motional state heating suppression can be expected for modes with OOP ion motion.^{8,34} A single Ca^+ ion heating rate of 8.6 ± 0.4 quanta s^{-1} for a $2\pi \times 1.94$ MHz trap frequency was measured in the trap used here, and although the heating rates of IP axial modes for multi-ion chains are expected to be slightly larger than this, they are not currently limiting gate fidelity.

Lastly, the excitation spectrum becomes increasingly dense in larger ion crystals, especially when including the effects of higher-order motional sidebands. Nearby transitions can lead to unwanted state couplings and subsequent gate errors. This consideration is especially pertinent in the $^{40}\text{Ca}^+ / ^{88}\text{Sr}^+$ system where the mass ratio $\mu = 2.2$ gives rise to a number of near-degeneracies, as shown in Methods.

A key example is the small energy splitting between the axial OOP mode first-order sideband and the axial IP-mode second-order sideband in this pair, due to the mode frequency ratio $\omega_{\text{OOP}}/\omega_{\text{IP}} = 1.988$. Driving the gate on the OOP mode is desirable in some cases, as it is affected less than the IP mode by motional heating. For a typical axial trap frequency of $\omega_{\text{IP}} \approx 2\pi \times 1$ MHz, the OOP-2IP splitting is only $2\pi \times 12$ kHz, approximately equal to typical detunings δ from the motional sidebands used during gate operations. Thus, a detuned drive of the OOP mode may be near resonant with the second-order IP sideband, potentially leading to error from unwanted displacement of this mode's motional state. This error is similar to off-resonant excitation of spectator modes on the first-order sideband,⁴⁶ although it depends on the different carrier Rabi frequencies and mode-dependent Lamb-Dicke parameters for each species and has an extra factor of the Lamb-Dicke parameter due to the higher-order excitation. We therefore expect the error to be (for small displacements and mode heating rates, and ignoring other off-resonant terms)

$$\epsilon_{2 \times \text{IP}} \approx |a|^2 \left(\bar{n}_{\text{IP}} + \frac{1}{2} \right) \quad (3)$$

where \bar{n}_{IP} is the average occupation of the IP mode before the gate and a is the displacement of the OOP mode due to the drive, expressed as (assuming IP excitation of the two ions at frequency ω)

$$a = \frac{1}{2} \int_0^{t_g} \left(\eta_{\text{Ca,IP}}^2 \Omega_{\text{Ca}} + \eta_{\text{Sr,IP}}^2 \Omega_{\text{Sr}} \right) e^{-i(\omega - 2\omega_{\text{IP}})t} dt. \quad (4)$$

Here, $\eta_{j,\beta}$ and Ω_j are the Lamb-Dicke parameter (see Methods for the definition in the multi-species case) and carrier Rabi frequency, respectively, for ion j in mode β , and t_g is the MS gate time. Evaluating this integral, we obtain

$$|a|^2 = \frac{\left(\eta_{\text{Ca,IP}}^2 \Omega_{\text{Ca}} + \eta_{\text{Sr,IP}}^2 \Omega_{\text{Sr}} \right) \sin^2 \left[(\omega - 2\omega_{\text{IP}}) \frac{t_g}{2} \right]}{(\omega - 2\omega_{\text{IP}})^2}. \quad (5)$$

Applying this result to the worst-case scenario, which corresponds to on-resonant driving of the IP second-order sideband ($\omega =$

$\omega_{\text{OOP}} + \delta = 2\omega_{\text{IP}}$ for the drive near the blue sideband), and for the dual-species gate conditions $\eta_{\text{Ca, OOP}} \Omega_{\text{Ca}} = \eta_{\text{Sr, OOP}} \Omega_{\text{Sr}} = \delta/4$, we find $\alpha = (\delta t_g/8) (\eta_{\text{Ca,IP}}^2 / \eta_{\text{Ca, OOP}} + \eta_{\text{Sr,IP}}^2 / \eta_{\text{Sr, OOP}})$; the error for a gate that acquires a π phase due to displacement around one-loop on the OOP mode ($t_g = 2\pi/\delta$) would then be

$$\epsilon_{2 \times \text{IP}} = \frac{\pi^2}{16} \left(\bar{n}_{\text{IP}} + \frac{1}{2} \right) \left(\frac{\eta_{\text{Ca,IP}}^2}{\eta_{\text{Ca, OOP}}} + \frac{\eta_{\text{Sr,IP}}^2}{\eta_{\text{Sr, OOP}}} \right)^2. \quad (6)$$

Even assuming negligible initial population in the motional modes, this error can be substantial; for a $\omega_{\text{IP}} = 2\pi \times 1$ MHz axial mode in the ground state, the error would be $\epsilon_{2 \times \text{IP}} = 0.013$ for a $^{40}\text{Ca}^+ - ^{88}\text{Sr}^+$ crystal. Moreover, as can be seen from the functional form of the acquired displacement (Eq. 5 with $\omega = \omega_{\text{OOP}} + \delta$), the width in gate detuning of the effect of driving near this IP resonance is set by $2\omega_{\text{IP}} - \omega_{\text{OOP}}$, so small relative changes in detuning will not be effective in significantly reducing this error. It is therefore prudent to avoid such near coincidences, either via judicious choices of detuning and laser intensity if available (although this removes a degree of freedom often used to optimize gate operation), trap frequency, mode of operation, or isotopes of the ions in the chain (see Methods for the mode frequency ratios for several different isotope combinations of Ca^+ and Sr^+); the latter can be very effective, as the absolute mode frequency difference sets the relevant scale. In the work presented here, the modes used to execute the dual-species MS gates were chosen to be spectrally well separated from all other transitions for attainable gate speeds.

Single-species two-qubit gates

Single-species quantum-logic gates are performed with either two Ca^+ or two Sr^+ ions in the trap such that the ions form a linear crystal oriented along the trap axis, with ions spaced a few microns apart. After sideband cooling and state preparation as described above, the MS interaction is brought about by applying light detuned near the IP vibrational-mode sidebands of the $|1\rangle \rightarrow |0\rangle$ transition; two frequencies are simultaneously applied to a single-pass AOM to produce a bichromatic light field with components detuned by δ above the blue sideband and below the red sideband of the mode β to be driven. This bichromatic field can be thought of as a drive resonant with the qubit carrier transition, but modulated at the beat frequency $\omega_\beta + \delta$. The bichromatic field is coupled into a single-mode, polarization-maintaining optical fiber and directed to the ions. Starting from $|11\rangle$, the joint qubit state is coherently driven between $|11\rangle$ and $|00\rangle$ via multiple pathways through $|10\rangle$ and $|01\rangle$ using the joint motional state. If this evolution is stopped after a time t_g as described above, the ions will be in a coherent superposition of $|11\rangle$ and $|00\rangle$, nominally the Bell state $|\Phi_{+\phi}\rangle = \frac{1}{\sqrt{2}}(|00\rangle + e^{i\phi}|11\rangle)$ (the value of ϕ is can be adjusted via the phases of the AOM RF drive signals used to create the bichromatic field; it must have a constant relative phase relationship with following analysis pulses). We apply the bichromatic gate pulses with an additional asymmetric detuning, calibrated separately, to compensate for AC-Stark shifts from other electronic levels, and we also shape the pulse amplitude in time to minimize dependence on the initial bichromatic phase.²⁹

To characterize gate operation, we estimate the created Bell-state fidelity by measuring the four elements of the resulting two-qubit density matrix ρ that would be nonzero in the case of ideal creation of $|\Phi_{+\phi}\rangle$. The two diagonal elements are computed from the probabilities to measure $|00\rangle$ and $|11\rangle$ after the entangling gate operation, P_{00} and P_{11} , respectively. The state population measurements are typically repeated thousands of times to precisely determine these values. The off-diagonal elements are calculated using an auxiliary "parity-flipping" measurement in which a $\pi/2$ -pulse around an axis in the equatorial plane of the

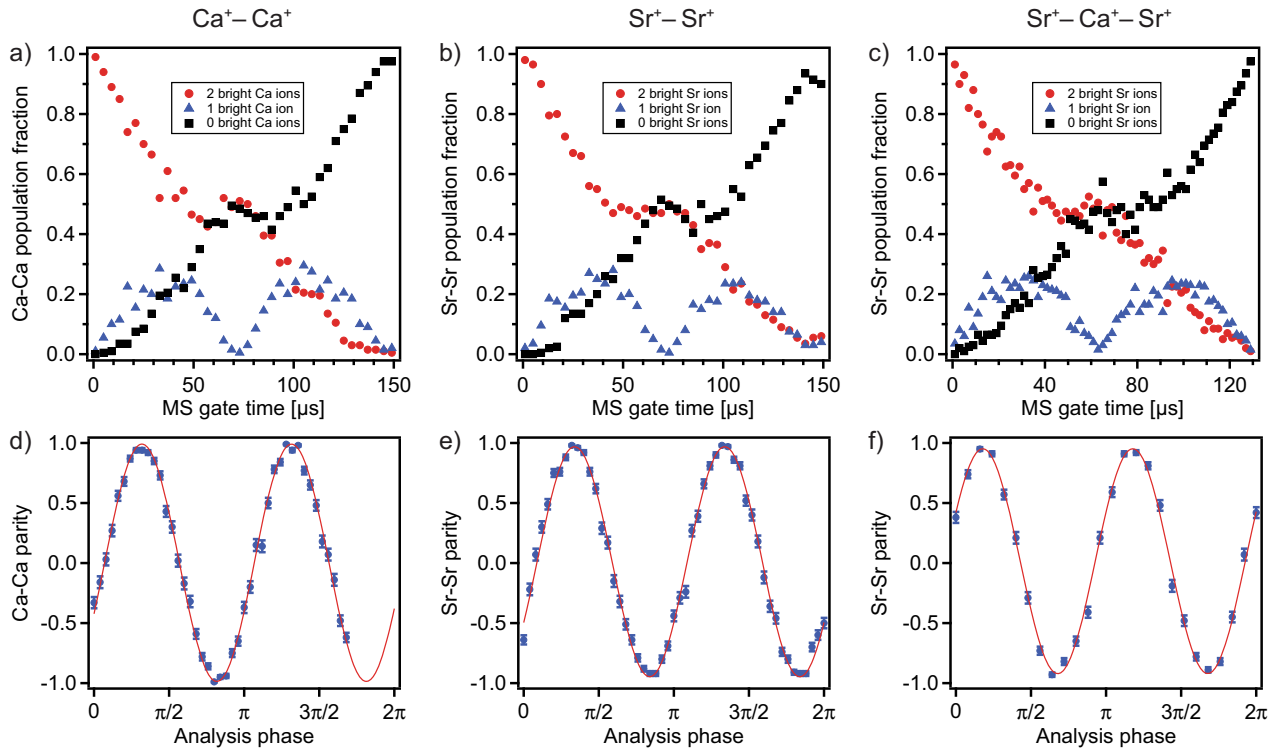


Fig. 3 Two-qubit entangling gates with ions of the same species. **a** Ca^+-Ca^+ Mølmer-Sørensen (MS) gate performed on the in-phase (IP) mode at $2\pi \times 1.2$ MHz; here, the measured state populations are plotted as a function of duration of the gate pulse. Starting with the product state $|11\rangle$ (two bright ions) at time 0, a maximally entangled state is created after $71 \mu\text{s}$. **b** Sr^+-Sr^+ MS gate performed on the IP mode at $2\pi \times 1.3$ MHz; the Bell state is created at a duration of $72 \mu\text{s}$. **c** MS gate on two Sr^+ ions with initial sympathetic cooling performed using a central Ca^+ ancilla, i.e., a $\text{Sr}^+-\text{Ca}^+-\text{Sr}^+$ three-ion chain; the IP-mode frequency is $2\pi \times 730$ kHz. The two Sr^+ ions are entangled after a gate duration of $61 \mu\text{s}$. **d** Parity-flopping curve for the Ca^+-Ca^+ gate shown in part (a). **e** Parity flopping curve for the Sr^+-Sr^+ gate shown in part (b). **f** Parity flopping curve for the $\text{Sr}^+-\text{Ca}^+-\text{Sr}^+$ gate shown in part (c). Lines in **d**, **e**, and **f** are sinusoidal fits to the data with constrained periods; the best-fit amplitude is used to calculate the Bell-state fidelity. The offset phases in these plots are related to ϕ and can be zeroed via adjustment of the bichromatic drive fields with respect to the carrier. Error bars reflect SEM

Bloch sphere of varying phase angle χ with respect to the X axis is applied uniformly to the ions in the created entangled state. This experiment effectively rotates the coherences into the populations and the parity of the populations, defined as $(P_{\chi,00} + P_{\chi,11}) - (P_{\chi,01} + P_{\chi,10})$, will oscillate with a period of π in χ for a two-qubit maximally entangled state. The amplitude C_{PF} of this oscillation gives a direct measure of the off-diagonal elements. We calculate the Bell-state fidelity as $F_{|\Phi_{+\phi}\rangle} \equiv \langle \Phi_{+\phi} | \rho | \Phi_{+\phi} \rangle = (P_{00} + P_{11} + C_{\text{PF}})/2$.

Figure 3 shows results for Ca^+ and Sr^+ single-species, two-qubit gates; both the measured state populations as a function of gate-interaction duration and the parity-flopping curves are shown. In the case of ideal evolution, the Bell state $|\Phi_{+\phi}\rangle$ is created at the second zero of the combined population of the $|10\rangle$ and $|01\rangle$ states (“1-bright”). As can be seen, this time was (coincidentally) just over $70 \mu\text{s}$ in both cases; the achieved Bell-state error is $1.2(2)\%$ and $2.5(2)\%$ for Ca^+-Ca^+ and Sr^+-Sr^+ , respectively. Leading error sources are believed to be due to state dephasing from cryocooler vibrations and laser phase fluctuations. Cryocooler vibrations, which bring about an oscillation in the trap, and hence ion, location on the $10\text{--}100$ nm scale with respect to the delivery optics can lead to shot-to-shot variations in the gate-laser phase at the ion location. The effects of these variations could be mitigated in future work by interferometrically stabilizing the optical path length to the ions.^{47,48} Laser instability is also a direct limit to optical qubit coherence time. From auxiliary measurements, we place an upper

limit on the laser bandwidth of 50 Hz, but due to cryocooler vibrations and variability of lab environmental parameters, we have measured coherence times at the $1\text{--}2$ ms level through single-ion Ramsey decay. Sources of error, which we expect to come in at a lower level, include intensity fluctuations, due to power fluctuations and beam pointing instability, which lead to variations of the Rabi frequency and fluctuating AC-Stark shifts due to additional levels in the ions’ electronic structure.

We have also performed an entangling quantum gate between two computational ions in the presence of a third ion of a different species, a primitive described above. Our implementation consists of an MS gate performed between two Sr^+ ions in a crystal with a $\text{Sr}^+-\text{Ca}^+-\text{Sr}^+$ configuration (see Fig. 2b). Initialization for these experiments begins with Doppler cooling using the Ca^+ ancilla and quenching of the $|0\rangle$ states of the computational Sr^+ ions to prepare them in $|11\rangle$, followed by resolved sideband cooling on the IP vibrational mode using the ancilla only. The gate is then performed with light resonant with the computational ions only, with the bichromatic field tuned near the IP mode, as in the Sr^+-Sr^+ gate described above. Figure 3 shows the gate flopping and parity-flopping curves for this gate; we achieve a Bell state with infidelity of $0.043(3)$ in $61 \mu\text{s}$. Beyond the sources of imperfection mentioned above when discussing the Sr^+-Sr^+ gate, additional error sources include mode coupling to the uncooled spectator modes, particularly the stretch mode in which the center Ca^+ ion does not participate.

Dual-species two-qubit gates

We have also demonstrated a dual-species MS entangling operation. To create the Bell state $|\Phi_{+\phi}\rangle$ between Ca^+ and Sr^+ in a two-ion crystal, we start by Doppler and resolved sideband cooling both the axial IP and OOP modes using the Sr^+ ion. Following optical pumping to bring the ions to the $|11\rangle$ state, we simultaneously apply two bichromatic light fields, one to couple the internal state of each species to the shared motion, each detuned from the IP vibrational mode (see Fig. 4a) by δ . The 674 nm and 729 nm beams are oriented parallel to the trap axis and anti-parallel to each other. As in the single-species case, we ramp up and down the pulse amplitude at the beginning and end of the interaction to avoid both dependence on the initial phase between the red- and blue-sideband drives and off-resonant excitation of the $|1\rangle \rightarrow |0\rangle$ carrier transition.²⁹

An additional consideration with MS gates on two different optical transitions on two different ion species is the relative phase of the force on each ion; this relationship is dictated by the relative phase of the red- and blue-sideband phase differences on each bichromatic beam pair at the ions' location. The distance between the ions ($\sim 3\ \mu\text{m}$) and the difference in the optical path lengths between the two bichromatic pairs ($\sim 100\ \text{mm}$) are both very small compared with the distance between maxima of the amplitude-modulated waveform of each bichromatic pair ($\sim 100\ \text{m}$, set by $\omega_\beta + \delta$, which is on the order of megahertz), so when the RF phases of the fields driving the AOMs producing the bichromatic fields are in phase, the force on the ions is as well. The four AOM RF drive signals, two each driving the 674 nm and 729 nm AOMs, are all phase coherent, derived from the same clock, allowing control and maintenance of shot-to-shot phase coherence of the force on the two ions. Although the 674 nm and 729 nm lasers each need to be coherent over the course of each experiment such that the analysis pulse phase (and that of any subsequent algorithmic logic pulses) is coherent with the beams driving the gate, the relative optical phase between the two lasers does not need to be constant; only the relative phase between the red- and blue-sideband component phase differences must be maintained.

We extract the parity contrast by scanning the phases of $\pi/2$ analysis pulses for Ca^+ and Sr^+ applied simultaneously after the completion of the MS gate. In Fig. 4b we plot a representative population-flopping curve (taken with a slightly higher Rabi frequency than in the dataset used to calculate the state fidelity) and in Fig. 4c the parity-flopping curve for which the produced Bell state has a measured error of 0.057(3) for a gate duration of $160\ \mu\text{s}$. The mixed-species gate speed is limited here by the achievable sideband Rabi frequency for the Ca^+ ion. The amplitude of the normalized eigenvector $b_{\text{Ca,IP}}$ and the corresponding Lamb-Dicke parameter $\eta_{\text{Ca,IP}}$ are significantly lower for the chosen IP mode than in the single-species chain (see Table 2 in Methods). We expect some level of rejection of gate-laser-field noise common to both ions in same-species gates. On the contrary, for dual-species gates, the ions are driven by different lasers. Hence, we expect that effects such as differential phase and amplitude noise between the 674 nm and 729 nm light at the ion positions, leading to phase-space displacement variation and additional fluctuating AC-Stark shifts, are the primary causes for the larger error in dual-species MS gates.

DISCUSSION

The achieved infidelities and gate times for the Ca^+/Sr^+ quantum-logic primitives demonstrated here are listed in Table 1 along with the previously reported quantum-logic-assisted readout for the same two species. The achieved error probabilities are not due to fundamental sources, and so we believe they can be reduced with technological improvements in qubit-laser frequency and amplitude stability at the ions' location. This, along with the relative

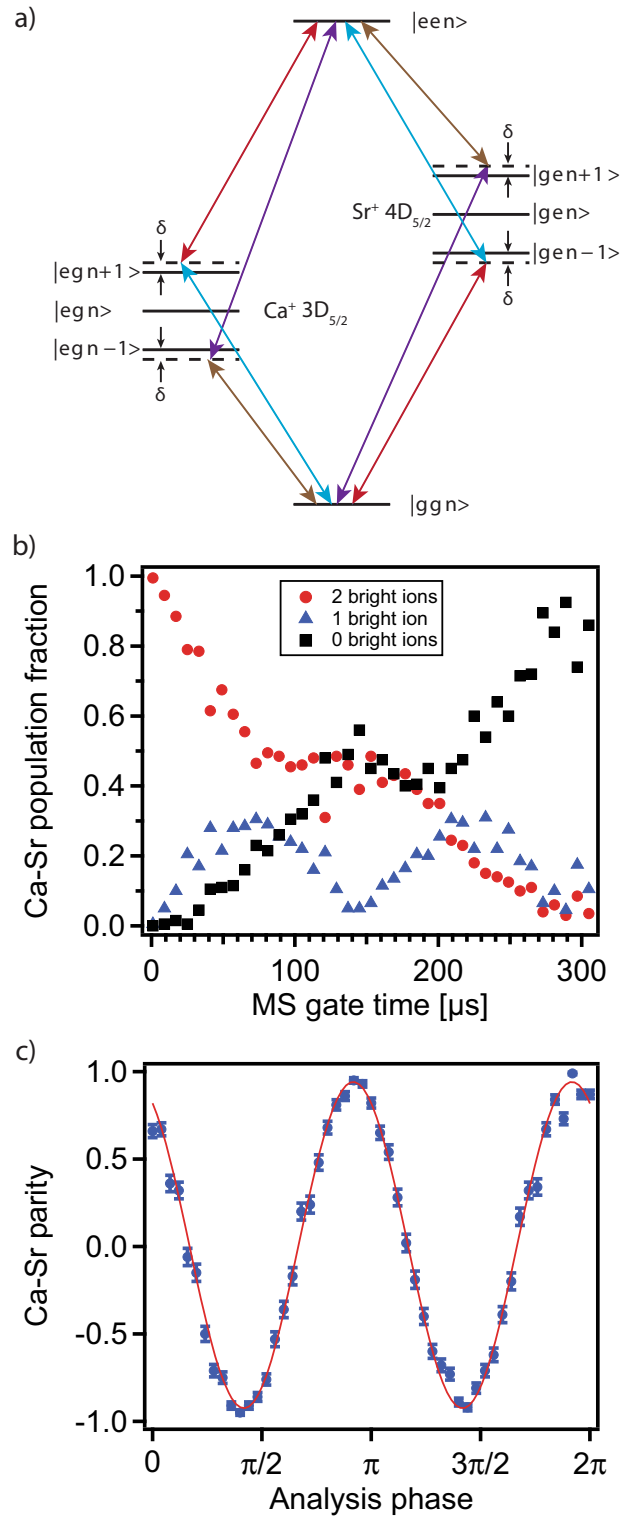


Fig. 4 Two-qubit entangling gate with ions of different species. **a** Level structure used in the Ca^+/Sr^+ Mølmer-Sørensen (MS) gate; The $|0\rangle, |1\rangle$ notation has been replaced with $|e\rangle, |g\rangle$ here to avoid confusion with the shared motional state occupation denoted by n . **b** Representative measured state populations are plotted as a function of duration of the gate pulse, here for a gate performed on the in-phase mode at $2\pi \times 770\ \text{kHz}$. A maximally entangled state is created here after $140\ \mu\text{s}$. The highest gate fidelities were achieved using a slightly lower Rabi frequency and correspondingly longer gate time of $160\ \mu\text{s}$. **c** Parity flopping for the $160\ \mu\text{s}$ gate, where the line is a sinusoidal fit with constrained period. Error bars reflect SEM

Table 1. Multi-qubit logic gates in the Ca⁺/Sr⁺ system in this and previous work

Species	Gate type	Mode frequency $\omega_{IP}/2\pi$ (MHz)	Gate time t_g (μ s)	Gate error $1 - F_{ \Phi_{\pm\phi}\rangle}$
Ca ⁺ –Ca ⁺	MS	1.2	71	0.012 (2)
Sr ⁺ –Sr ⁺	MS	1.3	72	0.025 (2)
Sr ⁺ –Ca ⁺ –Sr ⁺ (*)	MS	0.73	61	0.043 (3)
Ca ⁺ –Sr ⁺	MS	0.78	160	0.057 (3)
Ca ⁺ –Sr ⁺ (†)	QLS	1.3	96	0.04 (1)

Gate type, mode frequency, gate duration, and infidelity are listed for Mølmer-Sørensen (MS) gates (this work) and quantum-logic spectroscopy (QLS) transfer operation from Ca⁺ to Sr⁺ (previous work²²). *The gate was performed between the Sr ions with Ca used as a coolant ancilla. †The QLS transfer requires two consecutive sideband pulses; the total time is given. Also, QLS as demonstrated in ref. ²² maintains state populations only, hence here the inaccuracy (not infidelity) is reported

convenience of control methodologies for this pair of ion qubits, leads us to expect that these primitives will form the basis for more complex ancilla-assisted QIP in larger Ca⁺/Sr⁺ systems.

A notable aspect of multi-qubit operations in this particular system is the presence of optical-frequency qubits in both species, as we have demonstrated here. The presence of metastable *D* states allows for high-efficiency electron-shelving-based state detection, with the added potential for relatively lower optical power requirements for 10–100 μ s two-qubit gate durations when compared with Raman-based gates, or very low ultimate error rates for direct optical single- and two-qubit operations.⁷ In addition, Ca⁺ and Sr⁺ both possess optical qubits with qubit transition frequency in the red to near-infrared. This means that the control fields with the greatest requirements for optical power and frequency stability—those used for quantum gates—are at more technologically convenient wavelengths when compared with those used for Raman excitation, which are typically detuned from the higher-energy *S* \rightarrow *P* transitions. Optical elements such as crystals, fibers, and mirror coatings all perform better away from the ultraviolet. Furthermore, integrated waveguides and related photonics devices have lower loss at longer wavelengths,¹⁹ which is of particular interest for applications benefiting from control of large arrays of ions.

A consideration when employing ancilla ions of a different species from the logic ions is vibrational-mode structure. Driving coherent-displacement-based gates near accidental near-degeneracies should be avoided for the highest-fidelity logic-gate operation and, in some cases, species pairs may be chosen to avoid such coincidences. This appears to be straightforward for typical gate durations, but the problem could become more pronounced for high-speed operations, where more precisely tailored amplitude-shaped pulses may be required to account for driving multiple modes.³²

METHODS

Mode parameter calculation for dual-species ion chains and Lamb-Dicke parameters for various Ca⁺/Sr⁺ crystals

For the two-ion mixed-species chain, there are only two axial modes and their frequency ratio is given by:¹⁴

$$\frac{\omega_{OOP}}{\omega_{IP}} = \sqrt{\frac{1 + \mu + \sqrt{1 - \mu + \mu^2}}{1 + \mu - \sqrt{1 - \mu + \mu^2}}}, \quad (7)$$

where μ is the ion mass ratio, and ω_{IP} and ω_{OOP} are the frequencies of the IP and OOP normal modes, respectively. The ion-dependent Lamb-Dicke parameter for ion *j* with respect to the normal mode β is given by:⁴⁹

$$\eta_{j,\beta} = \sqrt{\frac{\hbar}{2m_j\omega_\beta}} \mathbf{k}_j \cdot \mathbf{b}_{j,\beta}, \quad (8)$$

where \mathbf{k}_j is the wavevector of the qubit laser, $\mathbf{b}_{j,\beta}$ is the normalized

motional eigenvector for ion *j* in normal mode β , ω_β is the oscillation frequency, m_j is the ion mass, and \hbar is the reduced Planck constant. The amplitudes of the motional eigenvectors $\mathbf{b}_{j,\beta}$ can be calculated numerically for arbitrary chain lengths and configurations.⁴⁹ In addition, simple closed form expressions exist for the two-ion chain;¹⁴ specifically, for ions *i, j*:

$$\mathbf{b}_{j,IP} = \sqrt{\frac{1 - \tilde{\mu} + \sqrt{1 - \tilde{\mu} + \tilde{\mu}^2}}{2\sqrt{1 - \tilde{\mu} + \tilde{\mu}^2}}}, \quad (9)$$

$$\mathbf{b}_{j,OOP}^2 = 1 - \mathbf{b}_{j,IP}^2,$$

where $\tilde{\mu}$ is the mass ratio expressed as $\tilde{\mu} = m_i/m_j$.

Analogous calculations of the normal mode frequencies and Lamb-Dicke parameters in a symmetric three-ion chain, such as the Sr⁺–Ca⁺–Sr⁺ chain used here, can also be made. The mode frequencies for a symmetric chain *i*₁–*j*–*i*₂ are given by⁸

$$\begin{aligned} \omega_{IP} &= \sqrt{\frac{13}{10} + \frac{21 - \sqrt{441 - 34\tilde{\mu}^{-1} + 169\tilde{\mu}^{-2}}}{10\tilde{\mu}^{-1}}} \omega_i, \\ \omega_{Stretch} &= \sqrt{3} \omega_i, \\ \omega_{Alt} &= \sqrt{\frac{13}{10} + \frac{21 + \sqrt{441 - 34\tilde{\mu}^{-1} + 169\tilde{\mu}^{-2}}}{10\tilde{\mu}^{-1}}} \omega_i, \end{aligned} \quad (10)$$

where ω_i is the axial frequency of a single ion with mass m_i . Here, $\omega_{Stretch}$ and ω_{Alt} are mode frequencies for the second, breathing-type axial mode and the third, alternating-ion-motion axial mode, respectively (see Fig. 2b). The definition of $\tilde{\mu}$ used here is the inverse of μ used in ref. ⁸ but has been chosen to be consistent with the convention used in the previous discussion of two-ion chains.

In contrast to the two-ion mixed-species chain, the normalized mode eigenvectors of a symmetric three-ion chain are dependent on the normal mode frequencies. These eigenvectors \mathbf{x}_β for ions *i*₁–*j*–*i*₂ in mode β can be calculated as⁸

$$\mathbf{x}_{IP} = N_{IP} \left(1, \frac{13 - 5(\omega_{IP}/\omega_i)^2}{8\sqrt{\tilde{\mu}}}, 1 \right), \quad (11)$$

$$\mathbf{x}_{Stretch} = N_{Stretch} (1, 0, -1), \quad (12)$$

$$\mathbf{x}_{Alt} = N_{Alt} \left(1, \frac{13 - 5(\omega_{Alt}/\omega_i)^2}{8\sqrt{\tilde{\mu}}}, 1 \right), \quad (13)$$

where $\mathbf{x}_\beta = (b_{i,\beta}, b_{j,\beta}, b_{i_2,\beta})$ and N_β are normalization constants. The Lamb-Dicke parameters can then be calculated using Eq. 8.

In Table 2, we list the mode parameters and Lamb-Dicke parameters (for a particular axial trap frequency) for dual-species, two- and three-ion crystals containing various common isotopes of Ca⁺ and Sr⁺. Besides allowing for the inclusion or exclusion of hyperfine structure in one or the other species, different isotopes lead to slightly different mode frequencies, providing the flexibility to avoid accidental overlaps between the target mode sidebands and higher-order sidebands of spectator modes. Small changes in mode frequencies can make a large difference as the relevant comparison is the frequency shift with the detuning from the sidebands, typically several kilohertz to a few tens of kilohertz (see main text).

Table 2. Selected mixed-species ion crystal parameters

Configuration	Axial mode β	$\omega_\beta/\omega_{\text{Sr}^+}$	$\omega_\beta/\omega_{\text{IP}}$	b_{Sr^+}	b_{Ca^+}	η_{Sr^+}	η_{Ca^+}
$^{40}\text{Ca}^+ - ^{88}\text{Sr}^+$	In-phase	1.137	1	0.902	0.431	0.074	0.048
	Out-of-phase	2.260	1.988	0.431	0.902	0.025	0.072
$^{40}\text{Ca}^+ - ^{88}\text{Sr}^+ - ^{40}\text{Ca}^+$	In-phase	1.232	1	0.781	0.441	0.061	0.047
	Stretch	2.569	2.085	0	0.707	0	0.052
	Alternating	2.898	2.352	-0.624	0.552	0.032	0.039
$^{88}\text{Sr}^+ - ^{40}\text{Ca}^+ - ^{88}\text{Sr}^+$	In-phase	1.095	1	0.652	0.385	0.054	0.044
	Stretch	1.732	1.582	0.707	0	0.047	0
	Alternating	3.262	2.979	0.272	-0.923	0.013	0.061
$^{43}\text{Ca}^+ - ^{88}\text{Sr}^+$	In-phase	1.129	1	0.892	0.453	0.073	0.049
	Out-of-phase	2.195	1.945	0.453	0.892	0.026	0.069
$^{43}\text{Ca}^+ - ^{88}\text{Sr}^+ - ^{43}\text{Ca}^+$	In-phase	1.215	1	0.765	0.455	0.060	0.048
	Stretch	2.478	2.040	0	0.707	0	0.052
	Alternating	2.836	2.335	-0.644	0.541	0.033	0.037
$^{88}\text{Sr}^+ - ^{43}\text{Ca}^+ - ^{88}\text{Sr}^+$	In-phase	1.089	1	0.648	0.400	0.054	0.044
	Stretch	1.732	1.590	0.707	0	0.047	0
	Alternating	3.164	2.905	0.283	-0.916	0.014	0.059
$^{40}\text{Ca}^+ - ^{86}\text{Sr}^+$	In-phase	1.134	1	0.899	0.438	0.074	0.049
	Out-of-phase	2.239	1.974	0.438	0.899	0.026	0.072
$^{40}\text{Ca}^+ - ^{86}\text{Sr}^+ - ^{40}\text{Ca}^+$	In-phase	1.227	1	0.776	0.446	0.062	0.048
	Stretch	2.540	2.070	0	0.707	0	0.053
	Alternating	2.878	2.346	-0.630	0.549	0.033	0.038
$^{86}\text{Sr}^+ - ^{40}\text{Ca}^+ - ^{86}\text{Sr}^+$	In-phase	1.093	1	0.651	0.390	0.055	0.044
	Stretch	1.732	1.584	0.707	0	0.047	0
	Alternating	3.230	2.955	0.276	-0.921	0.013	0.061
$^{43}\text{Ca}^+ - ^{86}\text{Sr}^+$	In-phase	1.126	1	0.888	0.460	0.074	0.050
	Out-of-phase	2.175	1.932	0.460	0.888	0.027	0.069
$^{43}\text{Ca}^+ - ^{86}\text{Sr}^+ - ^{43}\text{Ca}^+$	In-phase	1.209	1	0.760	0.460	0.061	0.048
	Stretch	2.449	2.026	0	0.707	0	0.052
	Alternating	2.818	2.331	-0.650	0.537	0.034	0.037
$^{86}\text{Sr}^+ - ^{43}\text{Ca}^+ - ^{86}\text{Sr}^+$	In-phase	1.087	1	0.646	0.405	0.054	0.045
	Stretch	1.732	1.594	0.707	0	0.047	0
	Alternating	3.133	2.883	0.286	-0.914	0.014	0.059

Calculated axial mode frequencies ω_β , normalized mode eigenvector amplitudes b_j , and associated Lamb-Dicke parameters η_j for mixed-species two-ion and symmetric three-ion chains made up of combinations of two different isotopes each of Ca^+ and Sr^+ . Frequencies are normalized by the single-ion frequency of the relevant Sr^+ isotope in the third column and normalized to the lowest frequency mode (ω_{IP}) for each ion configuration to highlight possible higher-order sideband degeneracies in the fourth column. To evaluate the Lamb-Dicke parameters, we calculate the necessary axial frequencies for $\omega_{\text{Sr}^+} = 2\pi \times 660 \text{ kHz}$, the corresponding single- Sr^+ trap frequency used for the dual-species gate demonstrated here. We also assume that the laser wavevector k_j is parallel to the ion motion

DATA AVAILABILITY

The data that support the findings of this study are available from the corresponding authors upon reasonable request.

Received: 3 July 2019; Accepted: 28 October 2019;

Published online: 21 November 2019

REFERENCES

- Kitaev, A. Y. Quantum measurements and the abelian stabilizer problem. Preprint at *arXiv:quant-ph/951106* (1995).
- Gottesman, D. & Chuang, I. L. Demonstrating the viability of universal quantum computation using teleportation and single-qubit operations. *Nature* **402**, 390 (1999).
- Nielsen, M. A. & Chuang, I. L. *Quantum Computation and Quantum Information* (Cambridge Univ. Press, 2000).
- Blatt, R. & Wineland, D. Entangled states of trapped atomic ions. *Nature* **453**, 1008 (2008).
- Monroe, C. & Kim, J. Scaling the ion trap quantum processor. *Science* **339**, 1164–1169 (2013).
- Bermudez, A. et al. Assessing the progress of trapped-ion processors towards fault-tolerant quantum computation. *Phys. Rev. X* **7**, 041061 (2017).
- Bruzewicz, C. D., Chiaverini, J., McConnell, R. & Sage, J. M. Trapped-ion quantum computing: progress and challenges. *Appl. Phys. Rev.* **6**, 021314 (2019).
- Kielpinski, D. et al. Sympathetic cooling of trapped ions for quantum logic. *Phys. Rev. A* **61**, 032310 (2000).
- Kielpinski, D., Monroe, C. & Wineland, D. J. Architecture for a large-scale ion-trap quantum computer. *Nature* **417**, 709 (2002).
- Nigg, D. et al. Quantum computations on a topologically encoded qubit. *Science* **345**, 302–305 (2014).
- Wang, Y. et al. Single-qubit quantum memory exceeding ten-minute coherence time. *Nat. Photonics* **11**, 646 (2017).
- Monroe, C. et al. Large-scale modular quantum-computer architecture with atomic memory and photonic interconnects. *Phys. Rev. A* **89**, 022317 (2014).

13. Tan, T. R. et al. Multi-element logic gates for trapped-ion qubits. *Nature* **528**, 380–383 (2015).
14. Wübbena, J. B., Amairi, S., Mandel, O. & Schmidt, P. O. Sympathetic cooling of mixed-species two-ion crystals for precision spectroscopy. *Phys. Rev. A* **85**, 043412 (2012).
15. Kielpinski, D., Volin, C., Streed, E. W., Lenzini, F. & Lobino, M. Integrated optics architecture for trapped-ion quantum information processing. *Quantum Inform. Process.* **15**, 5315–5338 (2016).
16. Mehta, K. K. & Ram, R. J. Precise and diffraction-limited waveguide-to-free-space focusing gratings. *Sci. Rep.* **7**, 2019 (2017).
17. Ghadimi, M. et al. Scalable ion-photon quantum interface based on integrated diffractive mirrors. *npj Quantum Inform.* **3**, 4 (2017).
18. West, G. N. et al. Low-loss integrated photonics for the blue and ultraviolet regime. *APL Photonics* **4**, 026101 (2019).
19. Sorace-Agaskar, C. et al. Multi-layer integrated photonics from the ultraviolet to the infrared. *Proc. SPIE* **10510**, 105100D (2018).
20. Benhelm, J., Kirchmair, G., Roos, C. F. & Blatt, R. Towards fault-tolerant quantum computing with trapped ions. *Nat. Phys.* **4**, 463–466 (2008).
21. Akerman, N., Navon, N., Kotler, S., Glickman, Y. & Ozeri, R. Universal gate-set for trapped-ion qubits using a narrow linewidth diode laser. *New J. Phys.* **17**, 113060 (2015).
22. Bruzewicz, C. D. et al. High-fidelity, single-shot, quantum-logic-assisted readout in a mixed-species ion chain. Preprint at [arXiv:1706.05102](https://arxiv.org/abs/1706.05102) (2017).
23. Schmidt, P. O. et al. Spectroscopy using quantum logic. *Science* **309**, 749–752 (2005).
24. Rosenband, T. et al. Frequency ratio of Al^+ and Hg^+ single-ion optical clocks; metrology at the 17th decimal place. *Science* **319**, 1808–1812 (2008).
25. Negnevitsky, V. et al. Repeated multi-qubit readout and feedback with a mixed-species trapped-ion register. *Nature* **563**, 527 (2018).
26. Ballance, C. J. et al. Hybrid quantum logic and a test of Bell's inequality using two different atomic isotopes. *Nature* **528**, 384 (2015).
27. Inlek, I. V., Crocker, C., Lichtman, M., Sosnova, K. & Monroe, C. Multispecies trapped-ion node for quantum networking. *Phys. Rev. Lett.* **118**, 250502 (2017).
28. Nigmatullin, R., Ballance, C. J., de Beaudrap, N. & Benjamin, S. C. Minimally complex ion traps as modules for quantum communication and computing. *New J. Phys.* **18**, 103028 (2016).
29. Kirchmair, G. et al. Deterministic entanglement of ions in thermal states of motion. *New J. Phys.* **11**, 023002 (2009).
30. Ballance, C. J., Harty, T. P., Linke, N. M., Sepiol, M. A. & Lucas, D. M. High-fidelity quantum logic gates using trapped-ion hyperfine qubits. *Phys. Rev. Lett.* **117**, 060504 (2016).
31. Harty, T. P. et al. High-fidelity trapped-ion quantum logic using near-field microwaves. *Phys. Rev. Lett.* **117**, 140501 (2016).
32. Schäfer, V. M. et al. Fast quantum logic gates with trapped-ion qubits. *Nature* **555**, 75 (2018).
33. Shapira, Y., Shaniv, R., Manovitz, T., Akerman, N. & Ozeri, R. Robust entanglement gates for trapped-ion qubits. *Phys. Rev. Lett.* **121**, 180502 (2018).
34. Wineland, D. J. et al. Experimental issues in coherent quantum-state manipulation of trapped atomic ions. *J. Res. Natl. Inst. Stand. Technol.* **103**, 259–328 (1998).
35. Fowler, A. G., Mariantoni, M., Martinis, J. M. & Cleland, A. N. Surface codes: Towards practical large-scale quantum computation. *Phys. Rev. A* **86**, 032324 (2012).
36. Hume, D. B., Rosenband, T. & Wineland, D. J. High-fidelity adaptive qubit detection through repetitive quantum nondemolition measurements. *Phys. Rev. Lett.* **99**, 120502 (2007).
37. Chiaverini, J. & Sage, J. M. Insensitivity of the rate of ion motional heating to trap-electrode material over a large temperature range. *Phys. Rev. A* **89**, 012318 (2014).
38. Sedlacek, J. A. et al. Evidence for multiple mechanisms underlying surface electric-field noise in ion traps. *Phys. Rev. A* **98**, 063430 (2018).
39. Bruzewicz, C. D., McConnell, R., Chiaverini, J. & Sage, J. M. Scalable loading of a two-dimensional trapped-ion array. *Nat. Commun.* **7**, 13005 (2016).
40. Wang, S. X., Labaziewicz, J., Ge, Y., Shewmon, R. & Chuang, I. L. Demonstration of a quantum logic gate in a cryogenic surface-electrode ion trap. *Phys. Rev. A* **81**, 062332 (2010).
41. Gabrielse, G. et al. A superconducting solenoid system which cancels fluctuations in the ambient magnetic field. *J. Magn. Reson.* (1969) **91**, 564–572 (1991).
42. Sørensen, A. & Mølmer, K. Quantum computation with ions in thermal motion. *Phys. Rev. Lett.* **82**, 1971–1974 (1999).
43. Sackett, C. A. et al. Experimental entanglement of four particles. *Nature* **404**, 256–259 (2000).
44. Roos, C. F. Ion trap quantum gates with amplitude-modulated laser beams. *New J. Phys.* **10**, 013002 (2008).
45. Safronova, U. I., Safronova, M. S. & Johnson, W. R. Forbidden $M1$ and $E2$ transitions in monovalent atoms and ions. *Phys. Rev. A* **95**, 042507 (2017).
46. Ballance, C. J. *High-Fidelity Quantum Logic in Ca^+* . Ph.D. thesis, University of Oxford (2014).
47. Bergquist, J. C., Itano, W. M. & Wineland, D. J. Laser stabilization to a single ion. In *Frontiers in Laser Spectroscopy* 359–376 (North Holland, 1994).
48. Ma, L. S. et al. Delivering the same optical frequency at two places: accurate cancellation of phase noise introduced by an optical fiber or other time-varying path. *Optics Lett.* **19**, 1777–1779 (1994).
49. Home, J. P. Quantum science and metrology with mixed-species ion chains. In *Advances in Atomic, Molecular, and Optical Physics*, Vol. 62, 231–277 (Elsevier, 2013).

ACKNOWLEDGEMENTS

We thank Vladimir Bolkhovskiy for trap fabrication, George Fitch for layout assistance, and Peter Murphy, Chris Thoummaraj, and Karen Magoon for assistance with chip packaging. We are also grateful to Robert Niffenegger and Garrett Simon for comments on the manuscript. This work was sponsored by the Under Secretary of Defense for Research and Engineering under Air Force contract number FA8721-05-C-0002. Opinions, interpretations, conclusions, and recommendations are those of the authors and are not necessarily endorsed by the United States Government.

AUTHOR CONTRIBUTIONS

C.D.B., J.C., and J.M.S. conceived of the work. C.D.B. performed the experiments, with assistance from R.M. and J.S. C.D.B. analyzed the data. All authors discussed the results and contributed to writing the paper.

COMPETING INTERESTS

The authors declare no competing interests.

ADDITIONAL INFORMATION

Correspondence and requests for materials should be addressed to C.D.B. or J.C.

Reprints and permission information is available at <http://www.nature.com/reprints>

Publisher's note Springer Nature remains neutral with regard to jurisdictional claims in published maps and institutional affiliations.



Open Access This article is licensed under a Creative Commons Attribution 4.0 International License, which permits use, sharing, adaptation, distribution and reproduction in any medium or format, as long as you give appropriate credit to the original author(s) and the source, provide a link to the Creative Commons license, and indicate if changes were made. The images or other third party material in this article are included in the article's Creative Commons license, unless indicated otherwise in a credit line to the material. If material is not included in the article's Creative Commons license and your intended use is not permitted by statutory regulation or exceeds the permitted use, you will need to obtain permission directly from the copyright holder. To view a copy of this license, visit <http://creativecommons.org/licenses/by/4.0/>.

This is a U.S. government work and not under copyright protection in the U.S.; foreign copyright protection may apply 2019